

This discussion paper is/has been under review for the journal Atmospheric Chemistry and Physics (ACP). Please refer to the corresponding final paper in ACP if available.

A numerical study of back-building process in a quasi-stationary rainband with extreme rainfall over northern Taiwan during 11–12 June 2012

C.-C. Wang¹, B.-K. Chiou¹, G. T.-J. Chen², and H.-C. Kuo²

¹Department of Earth Sciences, National Taiwan Normal University, Taipei, Taiwan

²Department of Atmospheric Sciences, National Taiwan University, Taipei, Taiwan

Received: 2 September 2015 – Accepted: 23 October 2015 – Published: 19 November 2015

Correspondence to: C.-C. Wang (cwang@ntnu.edu.tw)

Published by Copernicus Publications on behalf of the European Geosciences Union.

ACPD

15, 32679–32722, 2015

A numerical study of back-building process

C.-C. Wang et al.

Title Page

Abstract

Introduction

Conclusions

References

Tables

Figures



Back

Close

Full Screen / Esc

Printer-friendly Version

Interactive Discussion



Abstract

During 11–12 June 2012, quasi-stationary linear mesoscale convective systems (MCSs) developed near northern Taiwan and produced extreme rainfall up to 510 mm and severe flooding in Taipei. Evident back-building (BB) process in these MCSs contributed to the extreme rainfall, and thus is investigated using a cloud-resolving model. Specifically, we seek answers to the question why the location about 15–30 km upstream from the old cell is often more favorable for new cell initiation without the cold pool mechanism in this subtropical event during the mei-yu season.

With a horizontal grid size of 1.5 km, the model successfully reproduced the linear MCS and the BB process, which is found to be influenced by both dynamical and thermodynamical effects. During initiation in a background with convective instability, new cells are associated with positive (negative) buoyancy below (above) due to latent heating (adiabatic cooling), which represent a gradual destabilization. At the beginning, the new development is close to the old convection, which provides stronger warming below and additional cooling at mid-levels from evaporation of condensates, thus yielding a more rapid destabilization. This enhanced upward decrease in buoyancy at a lower height eventually creates an upward perturbation pressure gradient force to drive further development along with the buoyancy itself. After the new cell has gain sufficient strength, a descending branch at the old cell's rear flank acts to separate the new cell to about 20 km upstream. Therefore, the advantages of the spot in the BB process can be explained.

1 Introduction

As a common type of mesoscale convective systems (MCSs) with a lifespan around 3–12 h, organized rainbands such as the squall lines are capable of producing persistent precipitation at high intensity, compared to ordinary, isolated, or scattered convection (e.g., Carbone, 1982; Bluestein and Jain, 1985; Rotunno et al., 1988; Browning, 1990;

A numerical study of back-building process

C.-C. Wang et al.

Title Page

Abstract

Introduction

Conclusions

References

Tables

Figures



Back

Close

Full Screen / Esc

Printer-friendly Version

Interactive Discussion



A numerical study of back-building process

C.-C. Wang et al.

Title Page

Abstract

Introduction

Conclusions

References

Tables

Figures



Back

Close

Full Screen / Esc

Printer-friendly Version

Interactive Discussion



Houze et al., 1990; Chen and Chou, 1993; LeMone et al., 1998; Parker and Johnson, 2000; Doswell, 2001; Johnson and Mapes, 2001; Sun and Lee, 2002; Weisman and Rotunno, 2004; Meng et al., 2013). When such rainbands are slow-moving and the embedded deep convective cells travel at small angles, i.e., almost parallel, to the line, multiple cells can pass through the same locations in succession to rapidly increase rainfall accumulation and the potential of flash floods (e.g., Maddox et al., 1979; Doswell et al., 1996; Brooks and Stensrud, 2000; Parker and Johnson, 2004). For the eastern two thirds of the United States, Schumacher and Johnson (2005, 2006) found that 66 % of extreme rainfall events there are caused by quasi-linear MCSs, among which 54 % are produced by only two modes in organization. The training line-adjoint stratiform (TL/AS) type often forms along (or north of) an east–west (E–W) aligned, pre-existing slow-moving surface boundary, and a series of embedded “training” cells move eastward (also Stevenson and Schumacher, 2014; Peters and Roebber, 2014; Peters and Schumacher, 2015). The second type is quasi-stationary back-building (BB) systems, which depend more on meso- and storm-scale forcing and processes. In BB lines, new cells form repeatedly on the upwind side at nearly the same location then move downstream, making the line as a whole almost stationary (also Chappell, 1986; Corfidi et al., 1996). Compared to the TL/AS type, the BB systems are smaller and more localized, and thus more difficult to predict (e.g., Schumacher and Johnson, 2005).

To repeatedly trigger new cells in BB MCSs at mid-latitudes, a well-known mechanism is through convectively-generated outflow boundary from downdrafts, i.e., at the leading edge of the cold pool (or the gust front) that extends into the upwind side (e.g., Doswell et al., 1996; Parker and Johnson, 2000; Corfidi, 2003; Schumacher and Johnson, 2005, 2009; Houston and Wilhelmson, 2007; Moore et al., 2012). Similar mechanisms for the BB process are also found in some events in the East Asia (e.g., H. Wang et al., 2014; Jeong et al., 2015). However, toward lower latitudes such as the subtropics and tropics, the environments may be less conducive to cold pool development (e.g., Tompkins, 2001). Some studies on extreme rainfall events in South China and Taiwan have shown that surface-based cold air produced by previous convection

A numerical study of back-building process

C.-C. Wang et al.

Title Page

Abstract

Introduction

Conclusions

References

Tables

Figures



Back

Close

Full Screen / Esc

Printer-friendly Version

Interactive Discussion



that had dissipated for hours or even in the day before, when impinged by the moist monsoonal flow, in particular the low-level jet (LLJ), can act to trigger new convection in succession (e.g., Zhang and Zhang, 2012; Xu et al., 2012; C.-C. Wang et al., 2014a; Luo et al., 2014). Such mechanisms by “cold domes,” however, are different from the lifting at gust fronts produced by coexisting, dissipating cells or those that had just dissipated, and the induced MCSs may be less organized if a linear forcing such as a front or low-level convergence zone is absent (e.g., Xu et al., 2012; C.-C. Wang et al., 2014b).

Even though the environments near Taiwan (and some other subtropical regions) are not favorable for strong cold pools mainly due to high moisture content at low levels (e.g., Tompkins, 2001; James and Markowski, 2010; Yu and Chen, 2011) as mentioned, BB MCSs are still found (e.g., Li et al., 1997). For these systems, the mechanism for upstream initiation of new cells at the end of the convective line, presumably also dominated by storm-scale processes as their US counterparts (Schumacher and Johnson, 2005), is not clear. Recently, the roles of pressure perturbation (p'), in particular the dynamical pressure perturbation (p'_d , e.g., Rotunno and Klemp, 1982; Weisman and Klemp, 1986; Klemp, 1987, and many others), in the evolution of convective cells inside the E–W BB rainbands associated with Typhoon Morakot (2009) and extreme rainfall (e.g., Wang et al., 2012) are examined by Wang et al. (2015a, hereafter referred to as WKJ15). They found that in the presence of an intense westerly LLJ, the interaction between updraft and vertical wind shear (e.g., Klemp, 1987) induces positive (negative) p'_d at the western (eastern) flank of the updraft below the jet-core level (with westerly shear) but a reversed pattern above (with easterly shear), and thus an upward-directed perturbation pressure gradient force (PGF) at the western (rear) flank (see e.g., Fig. 6 of WKJ15). This leads to a slow-down in the propagation speed of mature cells and promotes cell merger inside the rainbands, as often observed in quasi-linear multi-cell MCSs. A reduced speed of old cell and positive p'_d at its rear flank near the surface can also enhance convergence and contribute to upstream new cell initiation without the cold pool (WKJ15). Obviously, one question worth exploring is whether a mechanism

conditions in the pre-storm environment, the sounding at Panchiao (near Taipei City) is used. For the evolution of the MCS and the resulted rainfall, the vertical maximum indicator (VMI) composites of radar reflectivity and hourly data from the rain-gauge network (Hsu, 1998) in Taiwan, both provided by the CWB, are employed. The above observational data are used both for analysis and verification of model results.

2.2 The CReSS model and experiment

The Cloud-Resolving Storm Simulator (CReSS) is used for our numerical simulation, and it is a cloud-resolving model that employs a nonhydrostatic and compressible equation set and a height-based terrain-following vertical coordinate (Tsuboki and Sakakibara, 2002, 2007). Clouds are treated explicitly in CReSS using a bulk cold-rain microphysical scheme (Lin et al., 1983; Cotton et al., 1986; Murakami, 1990; Ikawa and Saito, 1991; Murakami et al., 1994) with a total of six species (vapor, cloud water, cloud ice, rain, snow, and graupel). Sub-grid scale processes parameterized include turbulent mixing in the planetary boundary layer (PBL), radiation, and surface momentum and energy fluxes (Kondo, 1976; Louis et al., 1981; Segami et al., 1989). With a single domain (no nesting), this model has been used to study a number of heavy-rainfall events around Taiwan during the mei-yu season (e.g., C.-C. Wang et al., 2005, 2011, 2014a, b; Wang and Huang, 2009) as well as for real-time forecasts (e.g., Wang et al., 2013, 2015b; Wang, 2015). The CReSS model is open to the research community upon request, and its further details can be found in the works referenced above and at http://www.rain.hyarc.nagoya-u.ac.jp/~tsuboki/cress_html/index_cress_jpn.html.

In this study, the simulation is performed using a horizontal grid spacing of 1.5 km and a grid dimension (x, y, z) of $1000 \times 800 \times 50$ (cf. Fig. 1, Table 1). Already described, the NCEP $0.5^\circ \times 0.5^\circ$ gridded final analyses serve as the initial and boundary conditions (IC/BCs) of the model run from 12:00 UTC 10 June to 12:00 UTC 12 June 2012 (for 48 h). At the lower boundary, real terrain at 30 s resolution (or $(1/120)^\circ$, roughly 900 m) and observed weekly sea surface temperature (SST, Reynolds et al., 2002) are pro-

A numerical study of back-building process

C.-C. Wang et al.

Title Page

Abstract

Introduction

Conclusions

References

Tables

Figures



Back

Close

Full Screen / Esc

Printer-friendly Version

Interactive Discussion



vided. The model configuration and major aspects of the experiment are summarized in Table 1.

2.3 Analysis of vertical momentum and pressure perturbations

To investigate the BB process taking place in the present case using model outputs, the methods below, following Wilhelmson and Ogura (1972), Rotunno and Klemp (1982), Klemp (1987), and Parker and Johnson (2004), are used to perform analysis on vertical momentum and pressure perturbations. With the background environment assumed to be in hydrostatic equilibrium, the vertical momentum equation can be written as

$$\frac{dw}{dt} = -\frac{1}{\rho} \frac{\partial p'}{\partial z} - \frac{\rho'}{\rho} g + F_z \approx -\frac{1}{\rho_0} \frac{\partial p'}{\partial z} - \frac{\rho'}{\rho_0} g + F_z \quad (1)$$

where all variables have their conventional meanings. Here, $\rho = \rho_0 + \rho'$, where ρ_0 is the background value and ρ' the perturbation part of ρ , and $B = -g(\rho'/\rho_0)$ is the buoyancy. Thus, the vertical acceleration is driven by an imbalance among the perturbation PGF, buoyancy, and turbulent mixing. The buoyancy is constituted by the gaseous effect and the drag of all condensates, and can be expressed as

$$B = -\frac{\rho'}{\rho_0} g = g \frac{\theta'_v}{\theta_{v0}} - g \sum q_x \quad (2)$$

where θ_v is the virtual potential temperature (and $\theta_v = \theta_{v0} + \theta'_v$) and its perturbation accounts for the gaseous effect, while q_x denotes the mixing ratio of any condensate species.

The perturbation pressure p' can be divided into the dynamical and buoyant components as $p' = p'_d + p'_b$, and the diagnostic pressure equations for the anelastic set, with

A numerical study of back-building process

C.-C. Wang et al.

Title Page

Abstract

Introduction

Conclusions

References

Tables

Figures



Back

Close

Full Screen / Esc

Printer-friendly Version

Interactive Discussion



friction omitted (e.g., Rotunno and Klemp, 1982; Parker and Johnson, 2004), are

$$\nabla^2 p'_b = \frac{\partial}{\partial z}(\rho_0 B) \text{ and} \quad (3)$$

$$\nabla^2 p'_d = -\rho_0 \left[\left(\frac{\partial u}{\partial x} \right)^2 + \left(\frac{\partial v}{\partial y} \right)^2 + \left(\frac{\partial w}{\partial z} \right)^2 - w^2 \frac{\partial^2}{\partial z^2}(\ln \rho_0) \right] - 2\rho_0 \left(\frac{\partial v}{\partial x} \frac{\partial u}{\partial y} + \frac{\partial u}{\partial z} \frac{\partial w}{\partial x} + \frac{\partial v}{\partial z} \frac{\partial w}{\partial y} \right) \quad (4)$$

5 where ∇^2 is the laplacian operator. In both equations, a maximum (minimum) in $\nabla^2 p'$ corresponds to a minimum (maximum) in p' itself. Equation (3) states that p'_b is related to the vertical gradient of the product of ρ_0 and B . On the RHS of Eq. (4), inside the brackets are extension terms which imply maximized p'_d in regions of nonzero divergence or deformation. The other terms inside the parentheses are shearing terms and
 10 imply minimized p'_d in regions of nonzero vorticity (Parker and Johnson, 2004). The shearing effects include those related to vertical wind shear ($\partial u/\partial z$ and $\partial v/\partial z$) associated with the LLJ, as reviewed in Sect. 1 for the Morakot case. After $\nabla^2 p'_b$ or $\nabla^2 p'_d$ is obtained from Eqs. (3) or (4), the relaxation method is used to solve the associated pressure perturbation through iteration.

15 To provide additional verification, a second, independent method is also used in this study to compute p' as in WKJ15. In this method, p' is separated from its background pressure (p_0), defined as

$$p_0(x, y, z, t) = \langle p \rangle(x, y, z) + \Delta p(z, t), \quad (5)$$

20 where $\langle p \rangle$ is the time-averaged pressure over a fixed period, and Δp is the deviation of the areal-mean pressure \bar{p} at any given instant from its time mean $\langle \bar{p} \rangle$, such that

$$\Delta p(z, t) = \bar{p}(z, t) - \langle \bar{p} \rangle(z). \quad (6)$$

A numerical study of back-building process

C.-C. Wang et al.

Title Page

Abstract

Introduction

Conclusions

References

Tables

Figures



Back

Close

Full Screen / Esc

Printer-friendly Version

Interactive Discussion



The Panchiao sounding (Fig. 3) in the Taipei metropolitan area (cf. Fig. 2c) at 12:00 UTC 11 June indicated very strong southwesterly flow throughout the lower troposphere, with a peak of 25 m s^{-1} near 925 hPa and a well-mixed temperature profile underneath. The convective available potential energy (CAPE) was 583 J kg^{-1} and sufficient to support deep convection, if the air parcel could overcome the convective inhibition (CIN) of 78 J kg^{-1} to reach free convection (after 789 hPa). Obviously, these conditions were soon met since heavy rainfall did occur in Taipei. Note also that the humidity was quite high below about 550 hPa, and a dry layer did not exist throughout the troposphere. Thus, with instability, the strong, deep, and moisture-laden southwesterly flow near and to the south of the mei-yu front was clearly very favorable for active convection and substantial rainfall (e.g., C.-C. Wang et al., 2014a).

3.2 The back-building rainband with extreme rainfall

Figure 4 presents the composite VMI radar reflectivity from the ground-based radars in Taiwan at 1 h intervals, and depicts the evolution of the rainbands causing the extreme rainfall in northern Taiwan. At 12:00 UTC 11 June (Fig. 4a), an intense ENE–WSW-oriented squall line, with peak reflectivity in convective elements $\geq 50 \text{ dBZ}$, already formed and was approaching northern Taiwan to within about 30 km, i.e., at some 80–100 km ahead of the surface mei-yu front (cf. Figs. 1 and 2a). With a bulging middle section and trailing stratiform, the squall line moved southward at about 15 km h^{-1} and into northern Taiwan by 14:00 UTC (Fig. 4b and c). During the following hours through 18:00 UTC, this squall line continued to advance slowly and into 25° N , so that much of the northern Taiwan was covered by echoes with high reflectivity (Fig. 4d–g), while the stratiform region gradually moved eastward, in agreement with the upper-level wind (cf. Fig. 3). After 18:00 UTC, the convection through northern Taiwan evolved into a narrow line that remained quasi-stationary for hours until 23:00 UTC (Fig. 4g–i), with evident back-building behavior toward the west (to be detailed later). Eventually, this linear MCS started to move south slowly and gradually away from the Taipei area after 00:00 UTC 12 June (Fig. 4m–o), likely in conjunction with the surface front with the arrival of the

northeasterly flow (cf. Fig. 2c and f). During the entire period of Fig. 4, the mountain interiors in central and southern Taiwan also received continuous rainfall from forced uplift of the strong LLJ by the topography (cf. Fig. 2a and c), and another squall line also approached southern Taiwan from the west and made landfall near 22:00 UTC 11 June (Fig. 4i–o). Nonetheless, the reflectivity over northern Taiwan was both very active and lengthy, and produced by two types of MCSs: the first was the squall line before 18:00 UTC 11 June and reminiscent to a TL/AS system, and the second was the quasi-stationary BB MCS after 18:00 UTC (Fig. 4).

The distributions of 6 h accumulated rainfall during 12:00–18:00 and 18:00–24:00 UTC 11 June are shown in Fig. 5a and b. While three distinct rainfall centers over northern, central, and southern Taiwan were produced in each period, the amount over northern Taiwan was the highest. The rainfall during 12:00–18:00 UTC was maximized along the northwestern coast and decreased inland (Fig. 5a), consistent with the MCS that moved in from the ocean (cf. Fig. 4). On the other hand, the rainfall was more concentrated during 18:00–24:00 UTC with almost an E–W alignment, and the center was right near the Taipei City (Fig. 5b). The peak amount during this later 6 h period was 311 mm, and an extreme value of 510 mm was recorded from the entire event.

While some BB behavior also occurred in the TL/AS-type squall line, it was more active in the quasi-stationary BB system after 18:00 UTC and can be well depicted by the radar VMI reflectivity every 10 min (Fig. 6). As marked by the short arrows, frequent BB activities can be spotted at the western end of the convective line or west of existing cells, and some of them were quite close to the northwestern coast of Taiwan. After formation, they moved at small angles from the ENE–WSW-oriented quasi-stationary line, repeatedly across northern Taiwan (Fig. 6). The resulted rainfall in Fig. 5b, with the maximum located inland near Taipei, also implies that many cells matured after they moved onshore, instead of over the ocean prior to landfall. Thus, even though the development of the two MCSs are undoubtedly tied to the forcing and low-level convergence associated with the front and LLJ near northern Taiwan at meso- α and meso- β scales, the BB process at convective scale was an important factor leading

A numerical study of back-building process

C.-C. Wang et al.

[Title Page](#)[Abstract](#)[Introduction](#)[Conclusions](#)[References](#)[Tables](#)[Figures](#)[Back](#)[Close](#)[Full Screen / Esc](#)[Printer-friendly Version](#)[Interactive Discussion](#)

to the extreme rainfall in Taipei, especially during the later 6 h period after 18:00 UTC. Also, the new BB cell is often found to develop about 15–30 km upstream from an old cell in Fig. 6. Thus, why this particular spot has an advantage over other locations for new cell initiation, rather than the more general mechanism of quasi-linear MCS development, is the scientific question that we wish to answer in this study. This question will be addressed through our numerical simulation results below.

4 Results of model simulation

4.1 Model result validation

As described in Sect. 2.2, our CReSS model simulation was performed from 12:00 UTC 10 June 2012 for 48 h using NCEP (0.5°) final analyses as IC/BCs, with a horizontal grid spacing of 1.5 km. The simulated winds and the front at an elevation of 549 m (close to 950 hPa) at 12:00 UTC 11 June ($t = 24$ h) and frontal positions every 6 h are shown in Fig. 2b and d. Compared to the observation and NCEP analyses (Figs. 1, and 2a, e), the simulated front in Fig. 2b is slightly too north, especially west of 120.5° E and over land in southeastern China, but the prefrontal LLJ is well captured, including the strong winds near northern Taiwan. Linked to the position error of the front at 12:00 UTC, the modeled front is also too north at 18:00 UTC, but its western segment over the strait advanced southward more rapidly to catch up with the NCEP analyses during the next 6 h (Fig. 2c and d). The segment east of Taiwan, however, is still too north at 00:00 UTC 12 June (cf. Fig. 2f) and the position error there does not improve until about 12 h later (Fig. 2c and d).

The model-simulated surface winds at 10 m height and column-maximum mixing ratio of total precipitation every 2 h during 12:00–22:00 UTC 11 June are shown in Fig. 7, which can be compared with the radar composites in Fig. 4. In the model, the squall line before 18:00 UTC is along and to the north of the near-surface front (Fig. 7a–d) and different from the training-line system ahead of the front in the observation.

height in both cross-sections, consistent with the direction of the upper-level winds and the evolution of stratiform area (cf. Figs. 3 and 4).

The results of $\nabla^2 p'$ obtained by the two different methods (by separation and from Eqs. 3 and 4) as described in Sect. 2.3 at two different heights near 0.8 and 3 km are compared in Fig. 11, also for 21:00 UTC as an example. In general, the patterns are very similar. At 0.8 km, negative $\nabla^2 p'$ (implying $p' > 0$) occurs near the updraft of B1 with positive $\nabla^2 p'$ (implying $p' < 0$) to the east near the downdraft (Fig. 11a and b). West of B1 where B2 is developing, positive (negative) $\nabla^2 p'$ is found to the south (north) of the near-surface convergence zone. Near 3 km, the updraft of B1 corresponds to $\nabla^2 p' > 0$ and $\nabla^2 p' < 0$ occurs to its western flank and further upstream over B2 (Fig. 11d and e). The laplacian of buoyancy pressure perturbation ($\nabla^2 p'_b$) alone computed from Eq. (3) closely resembles that of the total pressure perturbations at both levels (except perhaps a slight southward shift near the updraft of B1 at 0.8 km), implying a dominant role of p'_b over p'_d in this event. Nevertheless, Fig. 11 confirms that the two methods yield consistent results.

4.3 Analysis of pressure perturbations

To examine the distributions of pressure perturbations and their roles in the BB process in greater details, a series of vertical cross-sections through the updraft center of B1 at 5 km and the near-surface center of B2 from 20:00 to 21:00 UTC (each roughly 50 km in length, cf. Fig. 9), i.e., during the initiation stage of B2, are constructed. Here, the structures of $\nabla^2 p'$ are first presented, so as to better infer to the patterns of p' discussed later through Eqs. (3) and (4). At 20:00 UTC when signs of B2 are yet to appear (Fig. 12a), the updraft of B1 ($> 5 \text{ m s}^{-1}$) is more upright with downdrafts at both flanks ($> 1 \text{ m s}^{-1}$ at mid-level or above). At the backside (upstream) of the updraft, in particular, $\nabla^2 p'$ is positive at mid-level and negative both above and below, corresponding to $p' < 0$ and $p' > 0$, respectively (as labeled by “L” and “H”). Again, the pattern of $\nabla^2 p'$ is largely attributable to its buoyant ($\nabla^2 p'_b$) instead of dynamical component ($\nabla^2 p'_d$, Fig. 12b and c). Twenty minutes later at 20:20 UTC (Fig. 12d), the updraft of B1 strengthens to more

A numerical study of back-building process

C.-C. Wang et al.

Title Page

Abstract

Introduction

Conclusions

References

Tables

Figures



Back

Close

Full Screen / Esc

Printer-friendly Version

Interactive Discussion



than 8 ms^{-1} and becomes more tilted, but the basic pattern of $\nabla^2 \rho'$ at its western flank and the upstream region remains. At this time, the suppressing downdraft there weakens, and B2 is developing ($\sim 0.5 \text{ m s}^{-1}$) just west of the sinking motion and about 15 km upstream from the core of B1. This new development is associated with $\rho' < 0$ below 1 km and $\rho' > 0$ over 1–3 km, and the perturbations (and those of B1) are also mainly

At 20:40 UTC (Fig. 12g), B1 further strengthens and is even more tilted with height, and its associated downdraft below the mid-level ($> 2 \text{ ms}^{-1}$ near 4 km) now appears only at the eastern (downwind) side. The upward motion of B2 can now reach over 1 ms^{-1} and extends further upstream, while a layer of positive $\nabla^2 \rho'$ (implying $\rho' < 0$) forms near 5 km, again mainly from the buoyant effects (cf. Fig. 12h). The distribution of $\nabla^2 \rho'_d$ is only significant at both flanks of the updraft of B1 below about 3.5 km (and at its eastern flank near 5 km, Fig. 12i), which forms gradually as B1 intensifies (Fig. 12c and f). The configuration of positive (negative) ρ'_d at the rear (forward) flank of the updraft near 500 mm (below the jet level, cf. Fig. 10c) and a reversed pattern above (near 2–3 km) is consistent with the shearing (plus extension) effect (cf. Eq. 4), in agreement with WKJ15 and other earlier studies. However, since w and its horizontal gradient are weak near the surface, where the vertical wind shear is larger (also Fig. 10c), the value of $\nabla^2 \rho'_d$ is smaller than that in WKJ15. Also, due to the farther distance, a direct role played by the dynamical pressure perturbations in new cell initiation of B2 appears limited in the case here.

Both B1 and B2 intensify at 21:00 UTC, and the latter, peaking at about 1.5 ms^{-1} , can now reach 4 km while the layer of $\nabla^2 \rho' > 0$ above (near 5 km) also grows stronger (Fig. 12j). A downdraft at the upstream flank of B1 reappears at mid-levels and penetrates down to 3 km at this time, and acts to separate B2 from B1 (also Fig. 11d). Like earlier times since 20:20 UTC, the total pattern of $\nabla^2 \rho$ is mainly contributed by $\nabla^2 \rho'_d$ only near the base of B1 (below 1.5 km), and by $\nabla^2 \rho'_b$ everywhere else (Fig. 12k and l). Thus, the latter effect is consistently the more dominant one in the region of B2 during its initiation stage in the model.

A numerical study of back-building process

C.-C. Wang et al.

[Title Page](#)[Abstract](#)[Introduction](#)[Conclusions](#)[References](#)[Tables](#)[Figures](#)[Back](#)[Close](#)[Full Screen / Esc](#)[Printer-friendly Version](#)[Interactive Discussion](#)

and therefore is also enhanced by evaporative cooling of cloud droplets (Fig. 13d–l). Thus, the cooling and subsequently $B < 0$ (near 3 km) associated with B2 is not only by the adiabatic effect, but also by evaporation at an earlier stage of initiation, for example, around 20:20 UTC (Fig. 13d and e).

Upstream from B1, the near-surface warming and cooling above, with maxima near 1 km and 3–4 km, respectively, create a decrease in buoyancy with height ($\partial B/\partial z < 0$) that grows stronger with time near B2 (Fig. 13d, g, and j). Together with the (near) exponential decrease of ρ_0 upward, this condition leads to $\nabla^2 \rho'_b < 0$ in Eq. (3), and thus $\rho'_b > 0$ that peaks slightly above 1 km and intensifies through time, as obtained using the relaxation method (Sect. 2.3) and shown in Fig. 14 (middle column). The upward decrease of ρ'_b , as the major component of total ρ' , in turn produces an upward-directed buoyant PGF to help B2 develop further (Figs. 14, left and middle columns). Thus, the combined effect of buoyancy B (cf. Fig. 13, left column) and total perturbation PGF in the vertical (cf. Eq. 1) is upward acceleration of parcels in B2 (Fig. 14, right column) to eventually reach free ascent and ignite deep convection (near 21:20 UTC, cf. Fig. 9).

5 Discussion

In the previous section, the pressure perturbation and buoyancy, dominated by the thermodynamic effects (including both adiabatic and diabatic ones), as well as the resultant upward development at the initiation stage of cell B2 are examined (Figs. 11–14). The specific roles played by the old cell B1 in triggering B2, however, are still not fully clear. Therefore, we further compare the initiation of an isolated cell farther upstream, C1, where no existing cell is present nearby (cf. Fig. 9), with B1–B2 pair and discuss their differences. This allows us to identify the additional role of B1 to new cell triggering, and thus to the BB process about 15–30 km upstream of the old cell in the present case.

A numerical study of back-building process

C.-C. Wang et al.

Title Page

Abstract

Introduction

Conclusions

References

Tables

Figures



Back

Close

Full Screen / Esc

Printer-friendly Version

Interactive Discussion



and it decreases with height more rapidly above, and three factors linked to the old cell B1 contribute to the establishment of the upward-directed perturbation PGF. First, a stronger cooling occurs near 3 km above B2 (Fig. 13), at levels significantly lower than that above C1 (cf. Fig. 16), and this cooling is enhanced by evaporation of condensates near the western edge of B1 (besides adiabatic effect). Second, a more rapid and efficient warming also occurs closer to the surface at the early stage of B2, and this is helped by the stronger LHR near the bottom of B1 (cf. Fig. 13). Both these effects can be thought of as a more rapid destabilization that gives the new cell the potential for a faster development. Finally, the separation by the descending branch of the old cell, when such a descent can reach a lower elevation, also plays a role in leading to BB process about 20 km upstream in the present case, based on our numerical simulation results. In C1 where $B > 0$ is counteracted by a downward perturbation PGF, all three advantages are absent without a nearby old cell (Figs. 15 and 16).

6 Conclusion and summary

During 11–12 June 2012 in the mei-yu season, both TL/AS and BB MCSs developed in succession near northern Taiwan, and together produced extreme rainfall up to 510 mm overnight in the Taipei metropolitan area, causing serious flooding in many densely populated regions. Observations show that BB behavior occurred in these MCSs, especially evident in the second, E–W-aligned quasi-stationary linear MCS during 18:00–24:00 UTC 11 June (02:00–08:00 LST 12 June), and was an important factor contributing to the extreme rainfall and related hazards in Taipei. The numerical simulation using the CReSS model with a horizontal grid size of 1.5 km starting at 12:00 UTC 10 June successfully captured the development and evolution of the BB MCS (but with considerable position error for the preceding TL/AS system). Then, the model results are used to investigate the details of the BB process occurring specifically about 15–30 km upstream from old convective elements in this subtropical system, where the cold pool mechanism is not responsible for triggering new cells at the end of the line.

A numerical study of back-building process

C.-C. Wang et al.

Title Page

Abstract

Introduction

Conclusions

References

Tables

Figures



Back

Close

Full Screen / Esc

Printer-friendly Version

Interactive Discussion



Although the dynamic pressure perturbations (ρ'_d) from the interaction between the mature cells and the LLJ, with $\rho'_d > 0$ (< 0) at the rear (forward) flank of the updraft near the surface below the jet and a reversed pattern near 2–3 km above the jet, can cause the mature cells to slow-down slightly and enhance the low-level convergence upstream, their effects are weaker compared to those found in WKJ15 for a case of typhoon rainband, and a direct role in new cell initiation appears quite limited.

In the present event, the total pressure perturbations (ρ') in the vicinity of the new cell throughout the initiation stage are attributed more to their buoyant (ρ'_b) than dynamical component. Forced by the low-level convergence (parallel to the line) in a convectively unstable storm environment, the early development of new cells are associated with positive buoyancy ($B > 0$) by latent heating below and negative buoyancy ($B < 0$) by adiabatic cooling above, and this represents a gradual destabilization in their surrounding environment. By comparing the BB process with the initiation of an isolated cell, the additional and specific roles played by the old cell to trigger new convection at the end of the line can be identified. At the initial stage, the development is close to the mature cell, which provides stronger warming below (and closer to the surface) and also additional cooling above from evaporation of condensates at its rear side. The more rapid upward decrease in B produces a positive ρ'_b at a lower height and subsequently an upward-directed perturbation (buoyant) PGF that drives further development together with the positive buoyancy. Thus, the net effect of the additional warming/cooling is essentially a more rapid destabilization that gives the new cell a faster development. After some time when the new cell has gain sufficient strength, a descending branch appearing at the rear flank of the old cell acts to separate the new cell to about 20 km upstream. The new cell continues to strengthen there, and eventually deep convection is ignited. Thus, the above roles played by the existing old cells, largely thermodynamic in origin but also helped by dynamical and kinematic effects, can explain why the spot roughly 15–30 km upstream from the western end of quasi-linear MCSs in the subtropics has advantages over other locations for new cell initiation in their back-building process, even in the absence of cold pool mechanism.

Acknowledgements. The authors wish to acknowledge the CWB and NCEP in providing the various data used in this study, and the helps from Mr. C.-Y. Lee in programming, and Mr. K.-Y. Chen and Ms. S.-Y. Huang in making some of the figures. This study is jointly supported by the Ministry of Science and Technology of Taiwan under Grants MOST-103-2119-M-003-001-MY2 and MOST-103-2625-M-003-001-MY2.

References

- Bluestein, H. B. and Jain, M. H.: Formation of mesoscale lines of precipitation: severe squall lines in Oklahoma during the spring, *J. Atmos. Sci.*, 42, 1711–1732, 1985.
- Brooks, H. E. and Stensrud, D. J.: Climatology of heavy rain events in the United States from hourly precipitation observations, *Mon. Weather Rev.*, 128, 1194–1201, 2000.
- Browning, K. A.: Organization of clouds and precipitation in extratropical cyclones, in: *Extratropical Cyclones: The Erik Palmén Memorial Volume*, edited by: Newton, C. W. and Holopainen, E. O., *Am. Meteor. Soc.*, Boston, MA, USA, 129–153, 1990.
- Carbone, R. E.: A severe frontal rainband. Part I: Stormwide hydrodynamic structure, *J. Atmos. Sci.*, 39, 258–279, 1982.
- Chappell, C. F.: Quasi-stationary convective events, in: *Mesoscale Meteorology and Forecasting*, edited by: Ray, P., *Am. Meteor. Soc.*, Boston, MA, USA, 289–310, 1986.
- Chen, G. T.-J. and Chou, H.-C.: General characteristics of squall lines observed in TAMEX, *Mon. Weather Rev.*, 121, 726–733, 1993.
- Chen, G. T.-J., Wang, C.-C., and Lin, D. T.-W.: Characteristics of low-level jets over northern Taiwan in Mei-yu season and their relationship to heavy rain events, *Mon. Weather Rev.*, 133, 20–43, 2005.
- Corfidi, S. F.: Cold pools and MCS propagation: forecasting the motion of downwind-developing MCSs, *Weather Forecast.*, 18, 997–1017, 2003.
- Corfidi, S. F., Meritt, J. H., and Fritsch, J. M.: Predicting the movement of mesoscale convective complexes, *Weather Forecast.*, 11, 41–46, 1996.
- Cotton, W. R., Tripoli, G. J., Rauber, R. M., and Mulvihill, E. A.: Numerical simulation of the effects of varying ice crystal nucleation rates and aggregation processes on orographic snowfall, *J. Clim. Appl. Meteorol.*, 25, 1658–1680, 1986.

A numerical study of back-building process

C.-C. Wang et al.

Title Page

Abstract

Introduction

Conclusions

References

Tables

Figures



Back

Close

Full Screen / Esc

Printer-friendly Version

Interactive Discussion



A numerical study of back-building process

C.-C. Wang et al.

Title Page

Abstract

Introduction

Conclusions

References

Tables

Figures



Back

Close

Full Screen / Esc

Printer-friendly Version

Interactive Discussion



Doswell III, C. A.: Severe convective storms – an overview, in: Severe Convective Storms, Meteor. Monogr., No. 50, Am. Meteor. Soc., Boston, MA, USA, ISBN: 978-1-878220-41-7, 1–26, 2001.

Doswell III, C. A., Brooks, H. E., and Maddox, R. A.: Flash flood forecasting: an ingredients-based methodology, *Weather Forecast.*, 11, 560–581, 1996.

Houston, A. L. and Wilhelmson, R. B.: Observational analysis of the 27 May 1997 central Texas tornadic event. Part I: Prestorm environment and storm maintenance/propagation, *Mon. Weather Rev.*, 135, 701–726, 2007.

Houze Jr., R. A., Smull, B. F., and Dodge, P.: Mesoscale organization of springtime rainstorms in Oklahoma, *Mon. Weather Rev.*, 118, 613–654, 1990.

Hsu, J.: ARMTS up and running in Taiwan, *Väisälä News*, 146, 24–26, 1998.

Ikawa, M. and Saito, K.: Description of a nonhydrostatic model developed at the Forecast Research Department of the MRI, MRI Tech. Rep. 28, Tsukuba, Japan, 238 pp., 1991.

James, R. P. and Markowski, P. M.: A numerical investigation of the effects of dry air aloft on deep convection, *Mon. Weather Rev.*, 138, 140–161, 2010.

Jeong, J.-H., Lee, D.-I., and Wang, C.-C.: A Study on an extreme rainfall-producing quasi-stationary mesoscale convective system over southeastern Korea: Impact of cold pool, *Mon. Weather Rev.*, revised, 2015.

Johnson, R. H. and Mapes, B. E.: Mesoscale processes and severe convective weather, in: Severe Convective Storms, edited by: Doswell III, C. A., Meteor. Monogr., No. 50, Am. Meteor. Soc., Boston, MA, USA, ISBN: 978-1-878220-41-7, 71–122, 2001.

Klemp, J. B.: Dynamics of tornadic thunderstorms, *Annu. Rev. Fluid Mech.*, 19, 369–402, 1987.

Kondo, J.: Heat balance of the China Sea during the air mass transformation experiment, *J. Meteorol. Soc. Jpn.*, 54, 382–398, 1976.

LeMone, M. A., Zipser, E. J., and Trier, S. B.: The role of environmental shear and thermodynamic conditions in determining the structure and evolution of mesoscale convective systems during TOGA COARE, *J. Atmos. Sci.*, 55, 3493–3518, 1998.

Li, J. and Chen, Y.-L.: Barrier jets during TAMEX, *Mon. Weather Rev.*, 126, 959–971, 1998.

Li, J., Chen, Y.-L., and Lee, W.-C.: Analysis of a heavy rainfall event during TAMEX, *Mon. Weather Rev.*, 125, 1060–1082, 1997.

Lin, Y.-L., Farley, R. D., and Orville, H. D.: Bulk parameterization of the snow field in a cloud model, *J. Clim. Appl. Meteorol.*, 22, 1065–1092, 1983.

**A numerical study of
back-building
process**

C.-C. Wang et al.

[Title Page](#)[Abstract](#)[Introduction](#)[Conclusions](#)[References](#)[Tables](#)[Figures](#)[Back](#)[Close](#)[Full Screen / Esc](#)[Printer-friendly Version](#)[Interactive Discussion](#)

- Louis, J. F., Tiedtke, M., and Geleyn, J. F.: A short history of the operational PBL – parameterization at ECMWF, in: Proceedings, ECMWF Workshop on Planetary Boundary Layer Parameterization, Reading, UK, 59–79, 1981.
- Luo, Y., Gong, Y., and Zhang, D.-L.: Initiation and organizational modes of an extreme-rain-producing mesoscale convective system along a Mei-yu front in East China, *Mon. Weather Rev.*, 142, 203–221, 2014.
- Maddox, R. A., Chappell, C. F., and Hoxit, L. R.: Synoptic and meso- α scale aspects of flash flood events, *B. Am. Meteorol. Soc.*, 60, 115–123, 1979.
- Meng, Z., Yan, D., and Zhang, Y.: General features of squall lines in East China, *Mon. Weather Rev.*, 141, 1629–1647, 2013.
- Moore, B. J., Neiman, P. J., Ralph, F. M., and Barthold, F. E.: Physical processes associated with heavy flooding rainfall in Nashville, Tennessee, and vicinity during 1–2 May 2010: the role of an atmospheric river and mesoscale convective systems, *Mon. Weather Rev.*, 140, 358–378, 2012.
- Murakami, M.: Numerical modeling of dynamical and microphysical evolution of an isolated convective cloud – the 19 July 1981 CCOPE cloud, *J. Meteorol. Soc. Jpn.*, 68, 107–128, 1990.
- Murakami, M., Clark, T. L., and Hall, W. D.: Numerical simulations of convective snow clouds over the Sea of Japan: two-dimensional simulation of mixed layer development and convective snow cloud formation, *J. Meteorol. Soc. Jpn.*, 72, 43–62, 1994.
- Parker, M. D. and Johnson, R. H.: Organizational modes of midlatitude mesoscale convective systems, *Mon. Weather Rev.*, 128, 3413–3436, 2000.
- Parker, M. D. and Johnson, R. H.: Structures and dynamics of quasi-2D mesoscale convective systems, *J. Atmos. Sci.*, 61, 545–567, 2004.
- Peters, J. M. and Roebber, P. J.: Synoptic control of heavy-rain-producing convective training episodes, *Mon. Weather Rev.*, 142, 2464–2482, 2014.
- Peters, J. M. and Schumacher, R. S.: Mechanisms for organization and echo training in a flash-flood-producing mesoscale convective system, *Mon. Weather Rev.*, 143, 1058–1085, 2015.
- Rotunno, R. and Klemp, J. B.: The influence of the shear-induced pressure gradient on thunderstorm motion, *Mon. Weather Rev.*, 110, 136–151, 1982.
- Rotunno, R., Klemp, J. B., and Weisman, M. L.: A theory for strong, long-lived squall lines, *J. Atmos. Sci.*, 45, 463–485, 1988.

A numerical study of back-building process

C.-C. Wang et al.

Title Page

Abstract

Introduction

Conclusions

References

Tables

Figures



Back

Close

Full Screen / Esc

Printer-friendly Version

Interactive Discussion



- Schumacher, R. S. and Johnson, R. H.: Organization and environmental properties of extreme-rain-producing mesoscale convective systems, *Mon. Weather Rev.*, 133, 961–976, 2005.
- Schumacher, R. S. and Johnson, R. H.: Characteristics of U. S. extreme rain events during 1999–2003, *Weather Forecast.*, 21, 69–85, 2006.
- 5 Schumacher, R. S. and Johnson, R. H.: Quasi-stationary, extreme-rain-producing convective systems associated with midlevel cyclonic circulations, *Weather Forecast.*, 24, 555–574, 2009.
- Segami, A., Kurihara, K., Nakamura, H., Ueno, M., Takano, I., and Tatsumi, Y.: Operational mesoscale weather prediction with Japan Spectral Model, *J. Meteorol. Soc. Jpn.*, 67, 907–924, 1989.
- 10 Stevenson, S. N. and Schumacher, R. S.: A 10-year survey of extreme rainfall events in the central and eastern United States using gridded multisensor precipitation analyses, *Mon. Weather Rev.*, 142, 3147–3162, 2014.
- Sun, J. and Lee, T.-Y.: A numerical study of an intense quasi-stationary convection band over the Korean Peninsula, *J. Meteorol. Soc. Jpn.*, 80, 1221–1245, 2002.
- 15 Tompkins, A. M.: Organization of tropical convection in low vertical wind shears: the role of cold pools, *J. Atmos. Sci.*, 58, 1650–1672, 2001.
- Tsuboki, K. and Sakakibara, A.: Large-scale parallel computing of cloud resolving storm simulator, in: *High Performance Computing*, edited by: Zima, H. P., Joe, K., Sato, M., Seo, Y., and Shimasaki, M., Springer-Verlag, Berlin and Heidelberg, Germany; New York, NY, USA, ISBN: 978-3-540-47847-8, 243–259, 2002.
- 20 Tsuboki, K. and Sakakibara, A.: Numerical Prediction of High-Impact Weather Systems: the Textbook for the Seventeenth IHP Training Course in 2007, Hydrospheric Atmospheric Research Center, Nagoya University and UNESCO, Nagoya, Japan, ISBN: 978-4-9980619-8-4, 273 pp., 2007.
- 25 Wang, C.-C.: The more rain, the better the model performs – The dependency of quantitative precipitation forecast skill on rainfall amount for typhoons in Taiwan, *Mon. Weather Rev.*, 143, 1723–1748, 2015.
- 30 Wang, C.-C. and Huang, W.-M.: High-resolution simulation of a nocturnal narrow convective line off the southeastern coast of Taiwan in the mei-yu season, *Geophys. Res. Lett.*, 36, L06815, doi:10.1029/2008GL037147, 2009.

**A numerical study of
back-building
process**

C.-C. Wang et al.

Title Page

Abstract

Introduction

Conclusions

References

Tables

Figures



Back

Close

Full Screen / Esc

Printer-friendly Version

Interactive Discussion



Wang, C.-C., Chen, G. T.-J., Chen, T.-C., and Tsuboki, K.: A numerical study on the effects of Taiwan topography on a convective line during the mei-yu season, *Mon. Weather Rev.*, 133, 3217–3242, 2005.

Wang, C.-C., Chen, G. T.-J., and Huang, S.-Y.: Remote trigger of deep convection by cold outflow over the Taiwan Strait in the Mei-yu season: a modeling study of the 8 June 2007 case, *Mon. Weather Rev.*, 139, 2854–2875, 2011.

Wang, C.-C., Kuo, H.-C., Chen, Y.-H., Huang, H.-L., Chung, C.-H., and Tsuboki, K.: Effects of asymmetric latent heating on typhoon movement crossing Taiwan: the case of Morakot (2009) with extreme rainfall, *J. Atmos. Sci.*, 69, 3172–3196, 2012.

Wang, C.-C., Kuo, H.-C., Yeh, T.-C., Chung, C.-H., Chen, Y.-H., Huang, S.-Y., Wang, Y.-W., and Liu, C.-H.: High-resolution quantitative precipitation forecasts and simulations by the Cloud-Resolving Storm Simulator (CRSS) for Typhoon Morakot (2009), *J. Hydrol.*, 506, 26–41, doi:10.1016/j.jhydrol.2013.02.018, 2013.

Wang, C.-C., Hsu, J. C.-S., Chen, G. T.-J., and Lee, D.-I.: A study of two propagating heavy-rainfall episodes near Taiwan during SoWMEX/TiMREX IOP-8 in June 2008. Part I: Synoptic evolution, episode propagation, and model control simulation, *Mon. Weather Rev.*, 142, 2619–2643, 2014a.

Wang, C.-C., Hsu, J. C.-S., Chen, G. T.-J., and Lee, D.-I.: A study of two propagating heavy-rainfall episodes near Taiwan during SoWMEX/TiMREX IOP-8 in June 2008. Part II: Sensitivity tests on the roles of synoptic conditions and topographic effects, *Mon. Weather Rev.*, 142, 2644–2664, 2014b.

Wang, C.-C., Kuo, H.-C., Johnson, R. H., Lee, C.-Y., Huang, S.-Y., and Chen, Y.-H.: A numerical study of convection in rainbands of Typhoon Morakot (2009) with extreme rainfall: roles of pressure perturbations with low-level wind maxima, *Atmos. Chem. Phys.*, 15, 11097–11115, doi:10.5194/acp-15-11097-2015, 2015a.

Wang, C.-C., Huang, S.-Y., Chen, S.-H., Chang, C.-S., and Tsuboki, K.: Cloud-resolving typhoon rainfall ensemble forecasts for Taiwan with large domain and extended range through time-lagged approach, *Weather Forecast.*, in press, doi:10.1175/WAF-D-15-0045.1, 2015b.

Wang, H., Luo, Y.-L., and Jou, B. J.-D.: Initiation, maintenance, and properties of convection in an extreme rainfall event during SCMREX: observational analysis, *J. Geophys. Res.-Atmos.*, 119, 13206–13232, doi:10.1002/2014JD022339, 2014.

A numerical study of back-building process

C.-C. Wang et al.

Title Page

Abstract

Introduction

Conclusions

References

Tables

Figures



Back

Close

Full Screen / Esc

Printer-friendly Version

Interactive Discussion



Weisman, M. L. and Klemp, J. B.: Characteristics of isolated convective storms, in: Mesoscale Meteorology and Forecasting, edited by: Ray, P. S., Am. Meteor. Soc., Boston, MA, USA, 331–358, 1986.

Weisman, M. L. and Rotunno, R.: “A theory for strong long-lived squall lines” revisited, J. Atmos. Sci., 61, 361–382, 2004.

Wilhelmson, R. B. and Ogura, Y.: The pressure perturbation and the numerical modeling of a cloud, J. Atmos. Sci., 29, 1295–1307, 1972.

Xu, W., Zipser, E. J., Chen, Y.-L., Liu, C., Liou, Y.-C., Lee, W.-C., and Jou, B. J.-D.: An orography-associated extreme rainfall event during TiMREX: Initiation, storm evolution, and maintenance, Mon. Weather Rev., 140, 2555–2574, 2012.

Yeh, H.-C., and Chen, Y.-L.: The role of offshore convergence on coastal rainfall during TAMEX IOP 3, Mon. Weather Rev., 130, 2709–2730, 2002.

Yu, C.-K. and Chen, Y.: Surface fluctuations associated with tropical cyclone rainbands observed near Taiwan during 2000–08, J. Atmos. Sci., 68, 1568–1585, 2011.

Zhang, M. and Zhang, D.-L.: Subkilometer simulation of a torrential-rain-producing mesoscale convective system in East China. Part I: Model verification and convective organization, Mon. Weather Rev., 140, 184–201, 2012.

A numerical study of back-building process

C.-C. Wang et al.

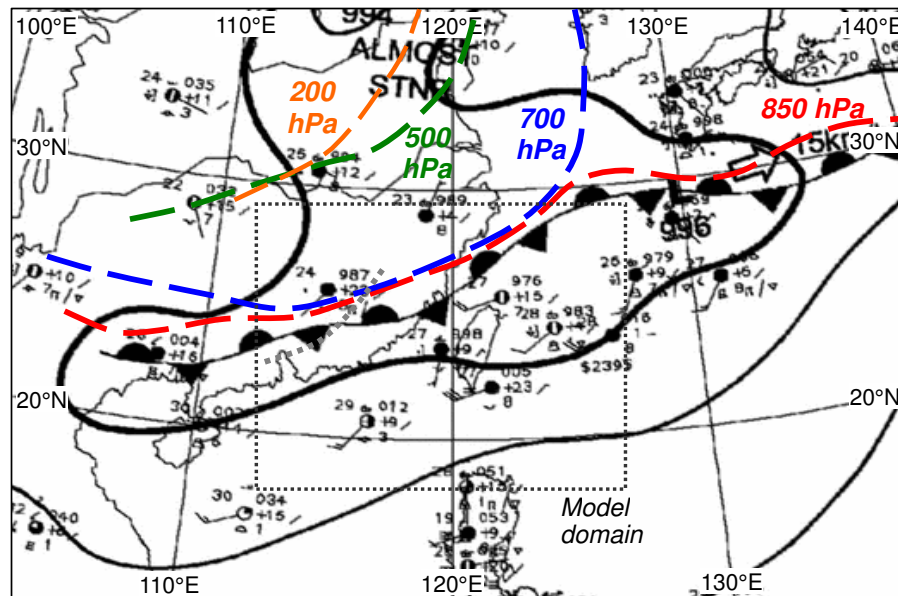


Figure 1. CWB surface analyses and positions of front/trough (or wind-shift line, thick dashed) at 850 (red), 700 (blue), 500 (green), and 200 hPa (orange) at 12:00 UTC 11 June 2012. The CReSS model domain is marked by the dotted box.

Title Page

Abstract

Introduction

Conclusions

References

Tables

Figures



Back

Close

Full Screen / Esc

Printer-friendly Version

Interactive Discussion



A numerical study of back-building process

C.-C. Wang et al.

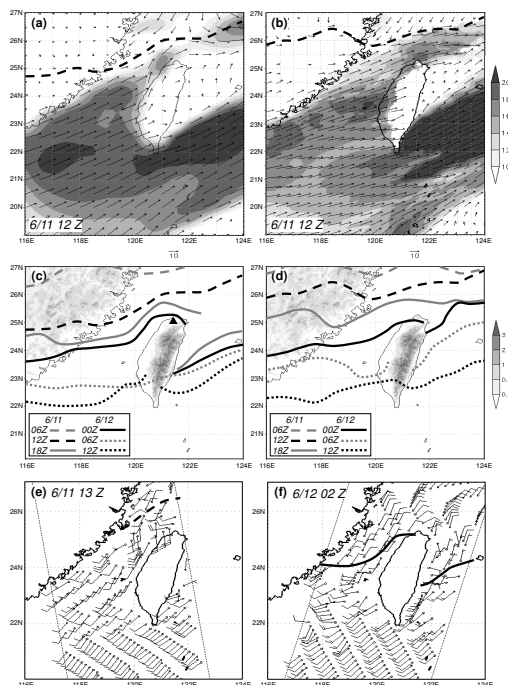


Figure 2. (a) NCEP (0.5°) 950 hPa analysis and (b) CReSS simulation of horizontal winds (ms^{-1} , speed shaded, scale to the right) at $z = 549$ m at 12:00 UTC 11 June 2012, with frontal position marked (thick dashed lines). (c, d) Frontal positions every 6 h from 06:00 UTC 11 June to 12:00 UTC 12 June 2012 (c) at 950 hPa in NCEP analyses and (d) at $z = 549$ m in model (see legend for line color and style), overlaid with topography (km, shading, scale to the right). The triangle in panel (c) marks the location of Panchiao sounding in Fig. 3. (e, f) ASCAT oceanic winds (ms^{-1}) near Taiwan at (e) 13:00 UTC 11 June and (f) 02:00 UTC 12 June, 2012, with surface frontal position analyzed.

A numerical study of back-building process

C.-C. Wang et al.

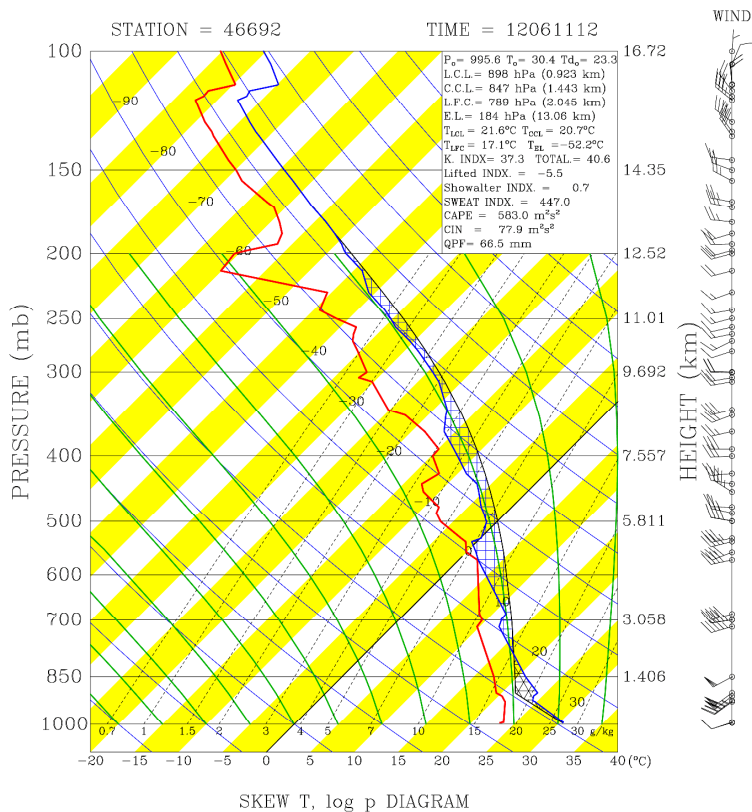


Figure 3. Thermodynamic (skew T -log p) diagram for the sounding taken at Panchiao (46692, cf. Fig. 2c for location) at 12:00 UTC 11 June 2012. For winds, full (half) barbs denote 10 (5) kts ($1 \text{ kt} = 0.5144 \text{ ms}^{-1}$), respectively.

Title Page

Abstract Introduction

Conclusions References

Tables Figures

◀ ▶

◀ ▶

Back Close

Full Screen / Esc

Printer-friendly Version

Interactive Discussion



A numerical study of back-building process

C.-C. Wang et al.

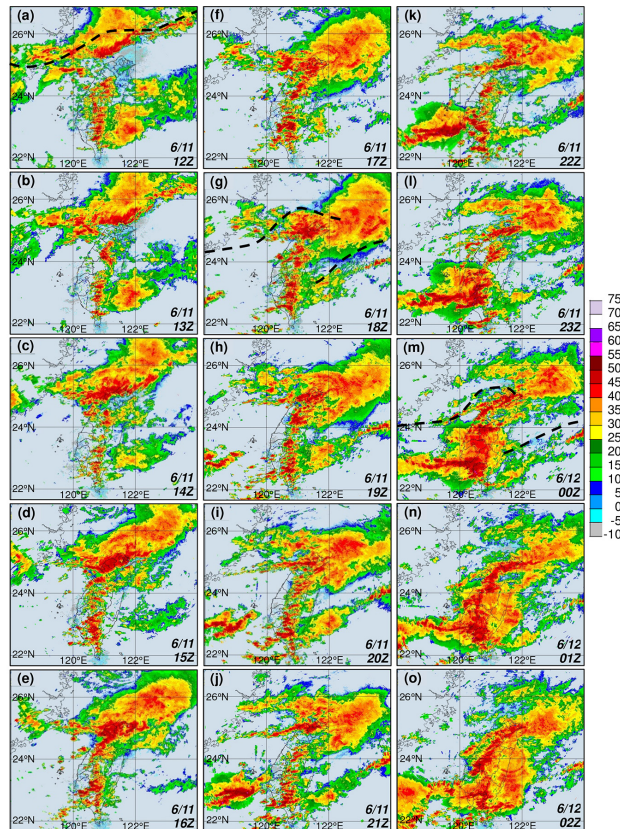


Figure 4. Composite VMI radar reflectivity (dBZ, color, scale to the right) over the Taiwan area at 1 h intervals from (a) 12:00 UTC 11 June to (i) 02:00 UTC 12 June, 2012.

[Title Page](#)
[Abstract](#)
[Introduction](#)
[Conclusions](#)
[References](#)
[Tables](#)
[Figures](#)
[◀](#)
[▶](#)
[◀](#)
[▶](#)
[Back](#)
[Close](#)
[Full Screen / Esc](#)
[Printer-friendly Version](#)
[Interactive Discussion](#)


A numerical study of back-building process

C.-C. Wang et al.

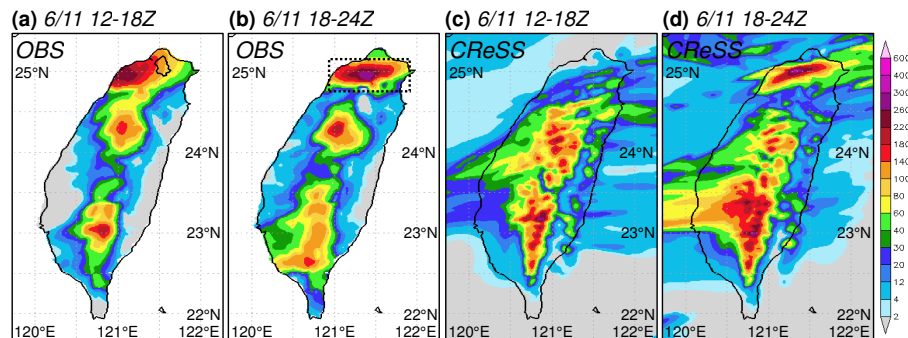


Figure 5. Distribution of observed 6 h accumulated rainfall (mm, color, scale to the right) over Taiwan during **(a)** 12:00–18:00 UTC and **(b)** 18:00–24:00 UTC 11 June 2012. The Taipei City boundary is depicted in panel **(a)**, and the dotted box in panel **(b)** shows the region used in Fig. 8 for rainfall average. **(c, d)** As in panels **(a, b)**, but showing model-simulated rainfall over Taiwan and the surrounding oceans.

[Title Page](#)[Abstract](#)[Introduction](#)[Conclusions](#)[References](#)[Tables](#)[Figures](#)[⏪](#)[⏩](#)[◀](#)[▶](#)[Back](#)[Close](#)[Full Screen / Esc](#)[Printer-friendly Version](#)[Interactive Discussion](#)

A numerical study of back-building process

C.-C. Wang et al.

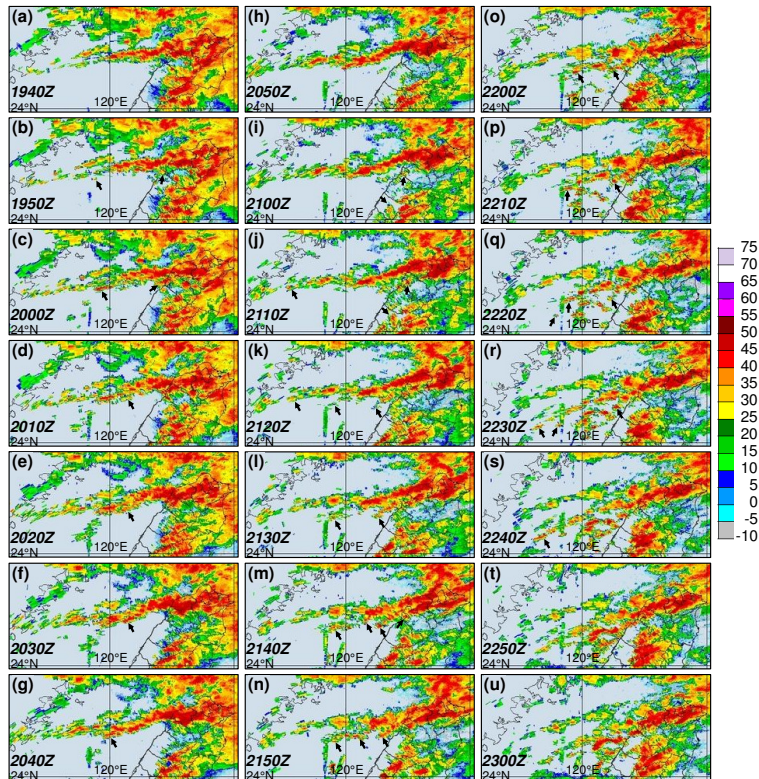


Figure 6. As in Fig. 4, but showing reflectivity over northern Taiwan and the upstream area every 10 min from (a) 19:40 UTC to (u) 23:00 UTC 11 June 2012. The arrows mark the initiation or strengthening of back-building cells.

[Title Page](#)
[Abstract](#)
[Introduction](#)
[Conclusions](#)
[References](#)
[Tables](#)
[Figures](#)
[Back](#)
[Close](#)
[Full Screen / Esc](#)
[Printer-friendly Version](#)
[Interactive Discussion](#)

A numerical study of back-building process

C.-C. Wang et al.

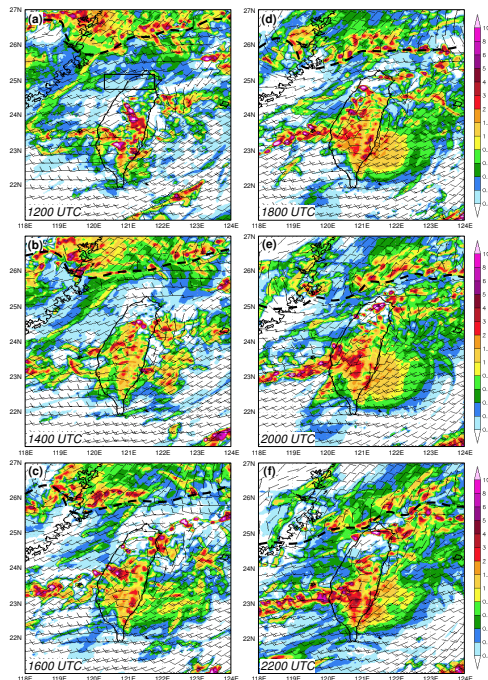


Figure 7. CReSS simulation of surface winds at 10 m height (m s^{-1}) and column-maximum mixing ratio of precipitation (rain + snow + graupel, g kg^{-1} , shading, scale to the right) every 2 h from (a) 12:00 UTC to (f) 22:00 UTC 11 June 2012. For winds, full (half) barbs denote 10 (5) m s^{-1} , and the surface frontal positions are marked (thick dashed lines). The rectangle in panel (a) depicts the area ($24.75\text{--}25.15^\circ \text{N}$, $120.35\text{--}121.75^\circ \text{E}$) used for the separation method.

A numerical study of back-building process

C.-C. Wang et al.

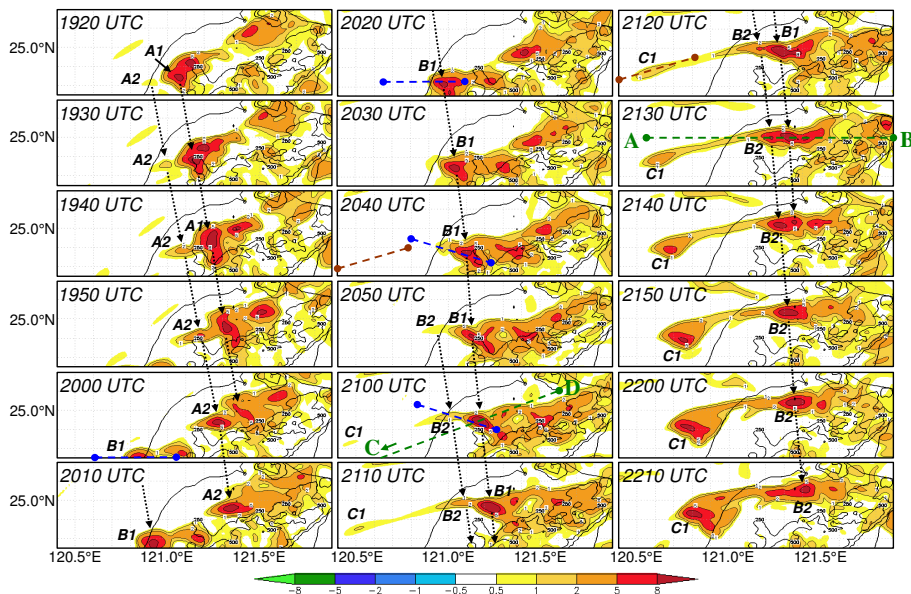


Figure 9. Model-simulated column-maximum vertical velocity (w , ms^{-1} , color and thin contours) every 10 min during 19:20–22:10 UTC 11 June 2012, overlaid with terrain elevation (m, thick contours at 250 and 500 m) in northern Taiwan. The color scale is shown at the bottom, and the contour at 0.5 ms^{-1} is not drawn. Old cells (A1, B1, and C1) and nearby new cells (A2, B2) of interests are labeled. Green dashed lines AB and CD depict the vertical cross-sections used in Fig. 10, and the short segments depict those used in Figs. 12–16 (blue (brown) ones through B1 (C1)).

Title Page

Abstract

Introduction

Conclusions

References

Tables

Figures



Back

Close

Full Screen / Esc

Printer-friendly Version

Interactive Discussion



A numerical study of back-building process

C.-C. Wang et al.

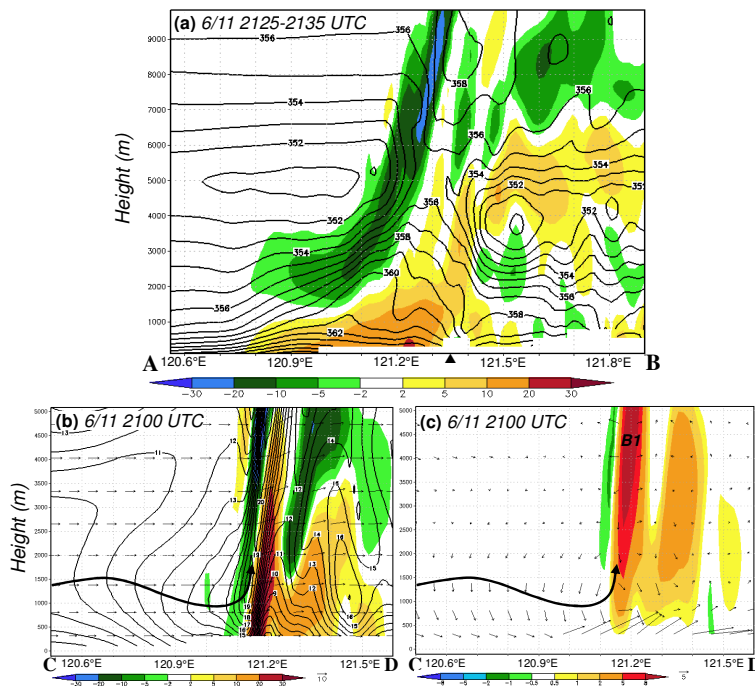


Figure 10. (a) E–W vertical cross-section of model-simulated convergence/divergence (10^{-4} s^{-1} , color, positive for convergence) and θ_e (K, contour, every 1 K) along 25° N (line AB in Fig. 9), averaged over 21:25–21:35 UTC 11 June 2012. The triangle depicts the mean location of the updraft of B1. (b, c) As in panel (a), except showing (b) convergence/divergence (color) and wind vectors (ms^{-1}) and (c) w (ms^{-1} , color) and vertical wind shear vector (10^{-3} s^{-1} , in cordinal direction, reference vectors both plotted) along the WSW–ENE section (line CD in Fig. 9) at 21:00 UTC 11 June 2012. Thick arrow-lines in panels (b, c) mark the axis of the LLJ.

A numerical study of back-building process

C.-C. Wang et al.

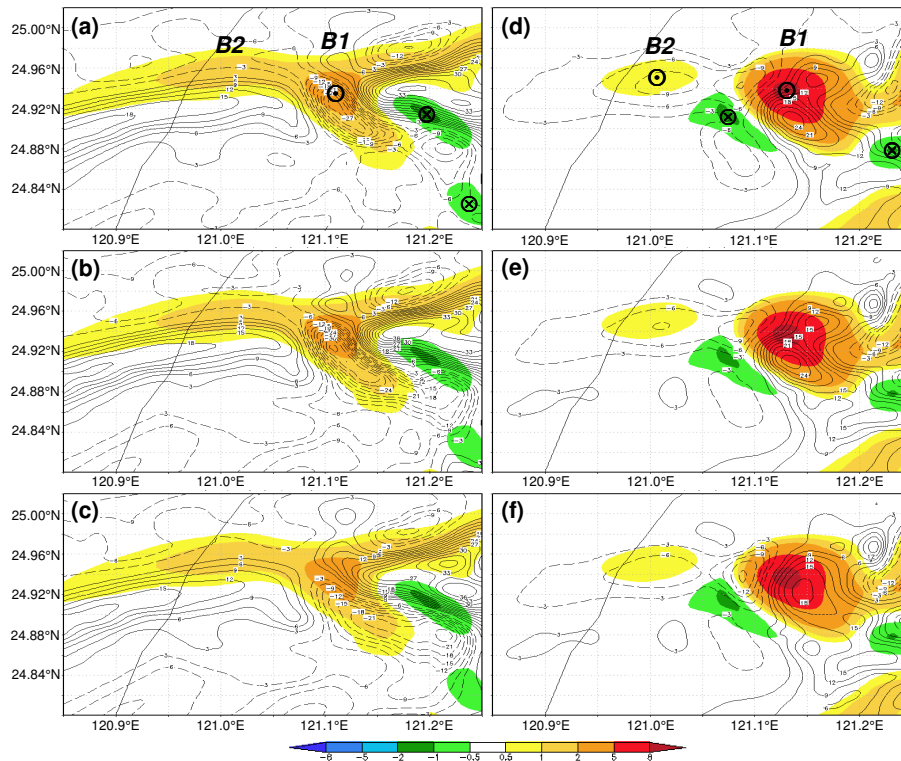


Figure 11. Model-simulated w (ms^{-1} , color, scale at bottom) and laplacian of perturbation pressure ($10^{-6} \text{ Pa m}^{-2}$, contour, every $3 \times 10^{-6} \text{ Pa m}^{-2}$, dashed for negative values) of cells B1 and B2 at (left) 806 m and (right) 2929 m at 21:00 UTC 11 June 2012. **(a, d)** $\nabla^2 p'$ obtained from separation method, and **(b, e)** $\nabla^2 p' = \nabla^2 p'_b + \nabla^2 p'_d$ and **(c, f)** $\nabla^2 p'_b$ computed from Eqs. (3) and (4). Cells B1 and B2 and updraft and downdraft centers are labeled in panels **(a)** and **(d)**.

Title Page	
Abstract	Introduction
Conclusions	References
Tables	Figures
◀	▶
◀	▶
Back	Close
Full Screen / Esc	
Printer-friendly Version	
Interactive Discussion	



A numerical study of back-building process

C.-C. Wang et al.

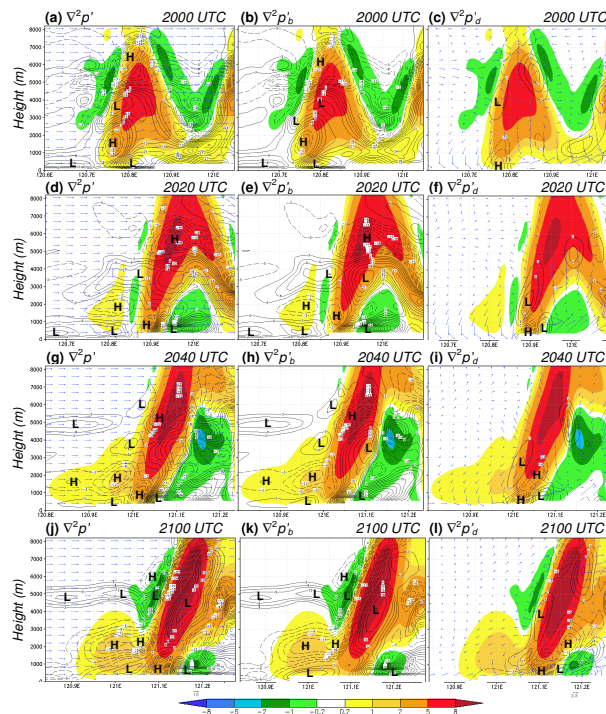


Figure 12. Vertical cross-sections of model-simulated w (ms^{-1} , color) and **(a)** $\nabla^2 p'$ (10^{-6}Pam^{-2}) and wind vectors (ms^{-1} , reference vector at bottom) on section plain, **(b)** $\nabla^2 p'_b$ (computed from Eq. 3), and **(c)** $\nabla^2 p'_d$ (computed from Eq. 4) and vertical wind shear vector (10^{-3}s^{-1} , in cardinal direction, reference vector at bottom) along the E–W segment through B1 and B2 at 20:00 UTC 11 June 2012 (cf. Fig. 9). All contour intervals are $3 \times 10^{-6} \text{Pam}^{-2}$ (zero line omitted, dashed for negative values), and letters H (L) denote corresponding high (low) pressure perturbations. **(d–f)**, **(g–i)**, and **(j–l)** As in panels **(a–c)**, except at 20:20, 20:40, and 21:00 UTC (WNW–ESE segments for 20:40 and 21:00 UTC, cf. Fig. 9), respectively.

A numerical study of back-building process

C.-C. Wang et al.

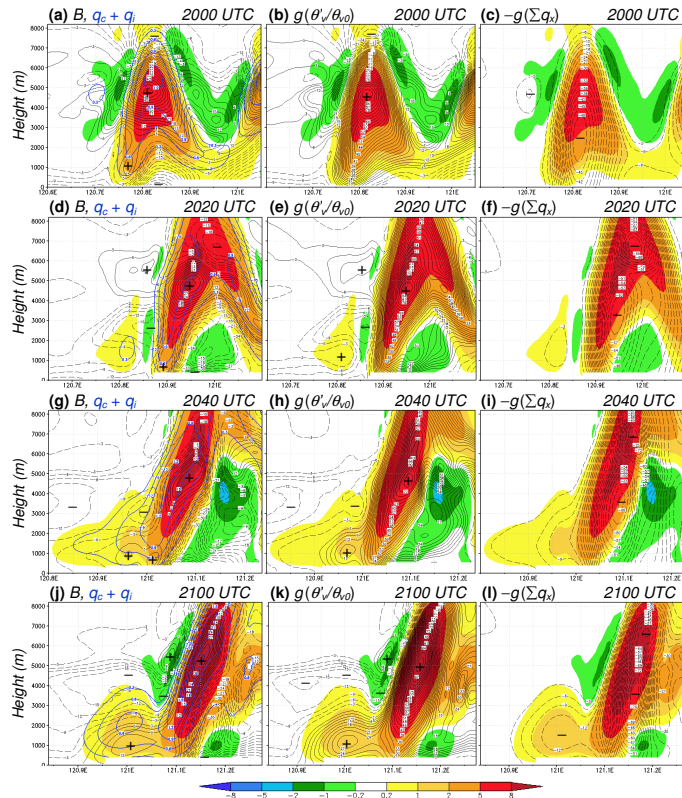


Figure 13. (a–c) As in Fig. 12a–c, but showing w and (a) buoyancy B (10^{-3} ms^{-2} , black contour) and mixing ratio of cloud particles (gkg^{-1} , blue contour, every 3 gkg^{-1}), (b) $g(\theta'_v/\theta_{v0})$ (10^{-3} ms^{-2}), and (c) $-g \sum q_x$ (10^{-3} ms^{-2}). All black contour intervals are $3 \times 10^{-6} \text{ Pam}^{-2}$ (dashed for negative values, zero line omitted), and + (–) signs denote upward (downward) maxima. (d–f), (g–i), and (j–l) As in panels (a–c), except at 20:20, 20:40, and 21:00 UTC, respectively.

[Title Page](#)
[Abstract](#)
[Introduction](#)
[Conclusions](#)
[References](#)
[Tables](#)
[Figures](#)
[Back](#)
[Close](#)
[Full Screen / Esc](#)
[Printer-friendly Version](#)
[Interactive Discussion](#)

A numerical study of back-building process

C.-C. Wang et al.

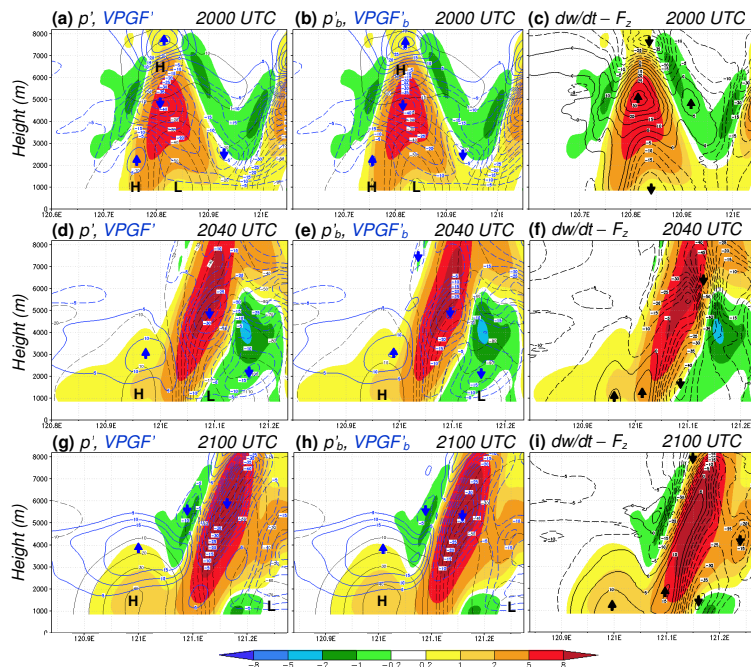


Figure 14. As in Fig. 13, but showing w and **(a, d, g)** $p' = p'_b + p'_d$ (Pa, black contour, every 10 Pa, dashed for negative values) obtained from the relaxation method and the corresponding perturbation PGF in the vertical $(-\partial p'/\partial z)/\rho_0$, 10^{-3} ms^{-2} , blue contour), **(b, e, h)** p'_b (Pa) and its vertical PGF (10^{-3} ms^{-2}), and **(c, f, i)** dw/dt from vertical perturbation PGF and B (10^{-3} ms^{-2} , black contour). For force (per unit mass) and acceleration, all contour intervals are $5 \times 10^{-3} \text{ ms}^{-2}$ (dashed for negative values), and upward (downward) arrows denote maxima (minima).

A numerical study of back-building process

C.-C. Wang et al.

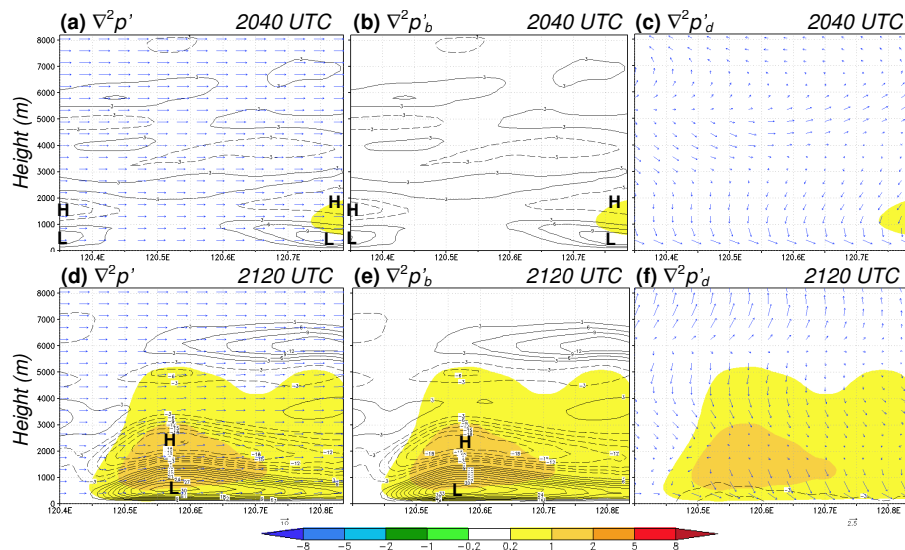


Figure 15. As in Fig. 12, but showing w (m s^{-1} , color) and **(a)** $\nabla^2 p'$ ($10^{-6} \text{ Pa m}^{-2}$) and wind vectors (m s^{-1}) on section plain, **(b)** $\nabla^2 p'_b$, and **(c)** $\nabla^2 p'_d$ and vertical wind shear vector (10^{-3} s^{-1} , in cardinal direction) along the WSW–ENE segment through C1 at 20:40 UTC 11 June 2012 (cf. Fig. 9). **(d–f)** As in panels **(a–c)**, except at 21:20 UTC.

Title Page

Abstract

Introduction

Conclusions

References

Tables

Figures



Back

Close

Full Screen / Esc

Printer-friendly Version

Interactive Discussion



A numerical study of back-building process

C.-C. Wang et al.

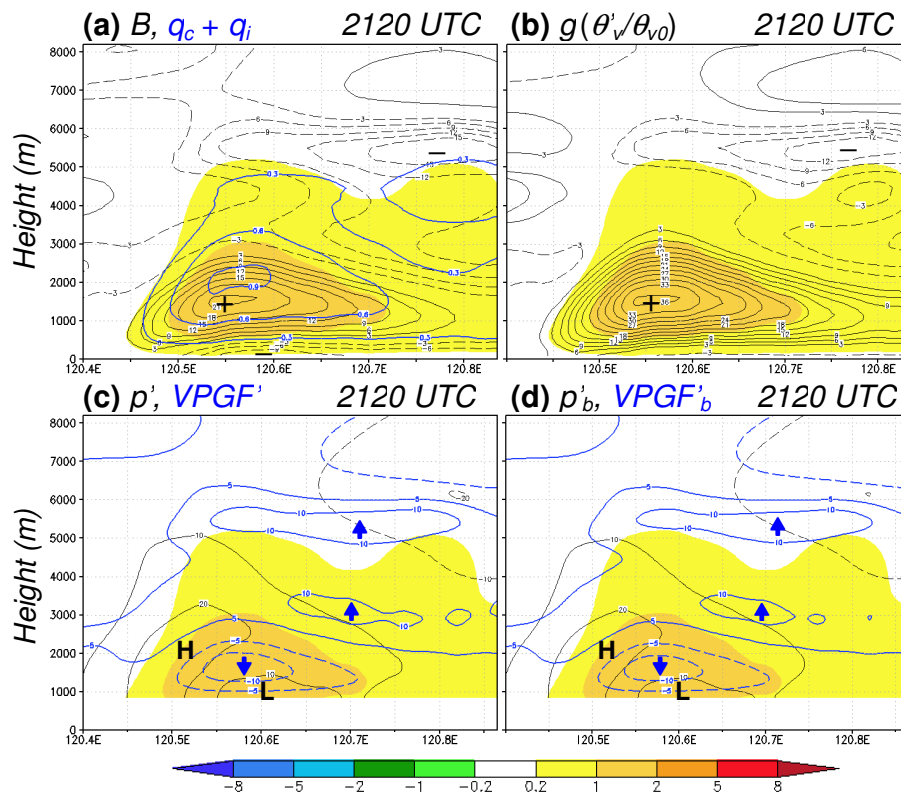


Figure 16. (a, b) As in Fig. 13a and b, but showing w (color) and (a) B (black contour) and mixing ratio of cloud particles (blue contour) and (b) $g(\theta'_v/\theta_{v0})$ along the WSW–ENE segment through C1 at 21:20 UTC 11 June 2012. (c, d) As in Fig. 14a and b, but showing w and (c) p' (black contour) obtain from the relaxation method and $-(\partial p'/\partial z)/\rho_0$ (blue contour) and (d) p'_b and its vertical PGF along the segment as in panels (a, b) at 21:20 UTC.

Title Page	
Abstract	Introduction
Conclusions	References
Tables	Figures
◀	▶
◀	▶
Back	Close
Full Screen / Esc	
Printer-friendly Version	
Interactive Discussion	

